Atmos. Meas. Tech., 6, 1633–1646, 2013
www.atmos-meas-tech.net/6/1633/2013/
doi:10.5194/amt-6-1633-2013

Atmospheric Measurement Techniques
Open Access

Averaging kernel prediction from atmospheric and surface state parameters based on multiple regression for nadir-viewing satellite measurements of carbon monoxide and ozone

H. M. Worden[1], D. P. Edwards[1], M. N. Deeter[1], D. Fu[2], S. S. Kulawik[2], J. R. Worden[2], and A. Arellano[3]

[1]National Center for Atmospheric Research (NCAR), Boulder, CO, USA
[2]Jet Propulsion Laboratory, California Institute of Technology, Pasadena, CA, USA
[3]University of Arizona, Tucson, AZ, USA

Correspondence to: H. M. Worden (hmw@ucar.edu)

Received: 21 February 2013 – Published in Atmos. Meas. Tech. Discuss.: 19 March 2013
Revised: 17 May 2013 – Accepted: 4 June 2013 – Published: 11 July 2013

Abstract. A current obstacle to the observation system simulation experiments (OSSEs) used to quantify the potential performance of future atmospheric composition remote sensing systems is a computationally efficient method to define the scene-dependent vertical sensitivity of measurements as expressed by the retrieval averaging kernels (AKs). We present a method for the efficient prediction of AKs for multispectral retrievals of carbon monoxide (CO) and ozone (O_3) based on actual retrievals from MOPITT (Measurements Of Pollution In The Troposphere) on the Earth Observing System (EOS)-Terra satellite and TES (Tropospheric Emission Spectrometer) and OMI (Ozone Monitoring Instrument) on EOS-Aura, respectively. This employs a multiple regression approach for deriving scene-dependent AKs using predictors based on state parameters such as the thermal contrast between the surface and lower atmospheric layers, trace gas volume mixing ratios (VMRs), solar zenith angle, water vapor amount, etc. We first compute the singular value decomposition (SVD) for individual cloud-free AKs and retain the first three ranked singular vectors in order to fit the most significant orthogonal components of the AK in the subsequent multiple regression on a training set of retrieval cases. The resulting fit coefficients are applied to the predictors from a different test set of test retrievals cased to reconstruct predicted AKs, which can then be evaluated against the true retrieval AKs from the test set. By comparing the VMR profile adjustment resulting from the use of the predicted vs. true AKs, we quantify the CO and O_3 VMR profile errors associated with the use of the predicted AKs compared to the true AKs that might be obtained from a computationally expensive full retrieval calculation as part of an OSSE. Similarly, we estimate the errors in CO and O_3 VMRs from using a single regional average AK to represent all retrievals, which has been a common approximation in chemical OSSEs performed to date. For both CO and O_3 in the lower troposphere, we find a significant reduction in error when using the predicted AKs as compared to a single average AK. This study examined data from the continental United States (CONUS) for 2006, but the approach could be applied to other regions and times.

1 Introduction

Atmospheric composition observation system simulation experiments (OSSEs) are valuable for assessing the potential information that would be provided by future satellite measurements and for quantifying the impact that these have on air quality characterization and forecasting. These simulations can be used for instrument design and mission planning in order to achieve an optimal configuration for the available cost. Chemical OSSEs have proved particularly useful for demonstrating the benefit of increased spatial and temporal (e.g., hourly) information obtained from geosynchronous Earth orbits (GEOs), as compared to low-Earth orbit (LEO) observations that are generally limited to a maximum of two observations of the same location twice per 24 h. Claeyman et al. (2011) employed OSSEs to investigate the

relative performance of different instrument options for a potential European GEO mission to characterize trace gas distributions. Using simulated measurements over North America from a GEO, OSSEs have demonstrated significant added capability compared to LEO observations for characterizing tropospheric carbon monoxide (CO) (Edwards et al., 2009) and ozone (O_3) (Zoogman et al., 2011). A goal of this study is the development of OSSEs for the Geostationary Coastal and Air Pollution Events (GEO-CAPE) mission (Fishman et al., 2012, and references therein), which is considering the use of multispectral measurements for CO and O_3, along with aerosols and other trace gases, for improving air quality models and understanding the interactions of atmospheric composition and climate change.

As described by Edwards et al. (2009), chemical OSSEs provide a way of expanding case-specific sensitivity studies into a more thorough quantification of the impact of future measurements in answering a critical science question. The basic procedure is as follows: (1) a chemical transport model is chosen that best represents the atmosphere and surface with the appropriate scales and physical processes relevant to the science goal. This model is used to perform a nature run (NR) that will represent the atmosphere true "nature" that we wish to characterize with the new measurement; (2) an instrument simulator is constructed for the candidate instrument concept and observing strategy. The instrument simulator is used to sample the NR to produce simulated retrieval products with associated errors and measurement characteristics; (3) a control run (CR) is defined to provide an alternative representation of the atmosphere, usually from a model that is different from the NR. The difference between the CR and NR atmospheres should be similar to the physical difference that might be expected between the prior atmospheric information that would be used as input to a retrieval scheme, such as a climatology, and the actual atmospheric state. (4) An assimilation run (AR) is performed with the CR as the starting point, in which the simulated measurements are assimilated. This mimics the way that future real data and operational retrievals might be used in a model analysis and forecast; (5) performance of the AR is evaluated by comparing to the CR. This provides a quantitative assessment of how well the assimilation of the simulated product drives the AR toward the NR.

The development of instrument simulators requires expert knowledge of measurement and data processing including instrument characterization, radiative transfer modeling and retrieval methods. Assuming that an inversion method according to Rodgers (2000) is used for the retrieval of a trace gas profile from a satellite measurement, then the vertical sensitivity of the retrieval with respect to the true atmospheric state is represented by the averaging kernel (AK), which embodies the full physics of the measurement and a description of the retrieval assumptions.

Following Rodgers (2000), the simulated trace gas measurement profile $\mathbf{x}_{\mathrm{sim}}$ can be written as

$$\mathbf{x}_{\mathrm{sim}} = \mathbf{A}\boldsymbol{x}_{\mathrm{NR}} + (\mathbf{I} - \mathbf{A})\boldsymbol{x}_{\mathrm{a}}, \tag{1}$$

where $\boldsymbol{x}_{\mathrm{NR}}$ is the "true" atmospheric profile as provided by the NR and $\boldsymbol{x}_{\mathrm{a}}$ is the a priori constraint profile. The averaging kernel matrix $\mathbf{A}$ is defined as

$$\mathbf{A} = \left(\mathbf{K}^T \mathbf{S}_{\mathrm{e}}^{-1}\mathbf{K} + \mathbf{S}_{\mathrm{a}}^{-1}\right)^{-1} \mathbf{K}^T \mathbf{S}_{\mathrm{e}}^{-1}\mathbf{K}, \tag{2}$$

where $\mathbf{S}_{\mathrm{e}}$ is the measurement error covariance, $\mathbf{S}_{\mathrm{a}}$ the a priori error covariance constraint used in the retrieval, and $\mathbf{K}$ the Jacobian matrix given by

$$\mathbf{K} = \frac{\partial \boldsymbol{F}}{\partial \boldsymbol{x}}, \tag{3}$$

which represents the sensitivity (weighting function) of forward model radiance $\boldsymbol{F}$ to physical state parameters $\boldsymbol{x}$. A useful quantity indicating the information content of the measurement is the degrees of freedom for signal (DFS), given by trace ($\mathbf{A}$) (Rodgers, 2000).

For accurate measurement simulation in an OSSE, a full radiative transfer forward model for radiance and Jacobians would be needed to compute AKs for each atmospheric and surface scene. Since this presents a computational burden, OSSE studies will often use average representations for the AK as an approximation (e.g., Edwards et al., 2009; Zoogman et al., 2011). This can lead to a mischaracterization of the instrument sensitivity, i.e., overestimation of sensitivity for some simulated measurements scenes and underestimation for others with the potential for regional biases in the OSSE results (Sellitto et al., 2013). Therefore, a method for quickly estimating the expected AK, given scene-dependent atmospheric and surface parameters for each simulated observation, is desired. A fast prediction scheme for scene-dependent AKs has been demonstrated in climate model evaluation with satellite measurements of deuterated water vapor (HDO) profiles (Field et al., 2012). However, overly simplified approximations may be insufficient, as shown by Sellitto et al. (2013) in their study of the limitations of applying a look-up-table (LUT) approach for estimating O_3 averaging kernels based only on thermal contrast.

Here we use multiple regression analysis of real satellite observations to estimate scene-dependent AKs. Multispectral retrievals of CO using the MOPITT (Measurements Of Pollution In The Troposphere) 4.6 µm thermal-infrared (TIR) and 2.3 µm near-infrared (NIR) channels are available in MOPITT V5 data (Worden et al., 2010; Deeter et al., 2011, 2012, 2013). Multispectral retrievals of O_3 retrievals that combine TIR and ultraviolet (UV) radiances have been shown with simulations (Worden et al., 2007; Landgraf and Hasekamp, 2007; Natraj et al., 2011) and recently demonstrated by Fu et al. (2013) using radiance measurements from the Tropospheric Emission Spectrometer

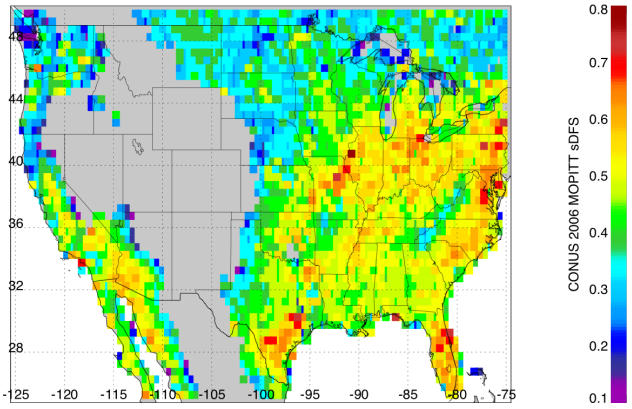

Fig. 1. MOPITT V5J sensitivity to near-surface CO, given by the trace of the AK for the lowest 3 layers, in $0.5° \times 0.5°$ bins. Only land scenes with surface pressure > 900 hPa are included, with higher altitudes, water and missing data indicated by grey or white.

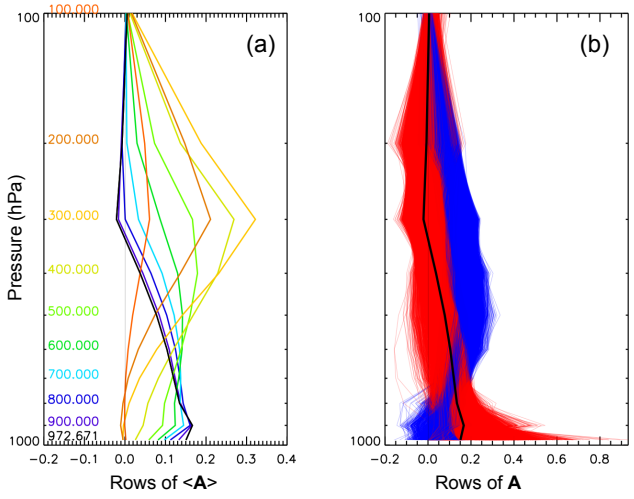

Fig. 2. MOPITT CO AKs for 2006 CONUS observations. **(a)** CONUS average AK, with colors corresponding to pressure levels indicated on the left. **(b)** Individual AK rows for 31 904 CONUS observations for the surface (red lines) and 500 hPa (blue lines) and average surface AK (black line).

(TES) and the Ozone Monitoring Instrument (OMI) and by Cuesta et al. (2013) with radiance measurements from the Infrared Atmospheric Sounding Interferometer (IASI) and the Global Ozone Monitoring Experiment-2 (GOME-2). Using retrievals of CO and O_3 over the continental United States (hereinafter referred to as CONUS) from 2006 observations, we divide the data into training and test sets, where the training sets are used in creating the multiple regression tool and the test sets are used for evaluation of the resulting AK prediction. This technique is presented as follows: Sect. 2 gives details of MOPITT and TES/OMI data selection; Sect. 3 describes the singular value decomposition (SVD) processing step; Sect. 4 presents the multiple regression fit of the singular vectors as a function of scene-dependent parameters; Sect. 5 shows the procedure for reconstructing predicted AKs from the multiple regression coefficients; Sect. 6 describes the metrics for evaluating the predicted AKs and the corresponding results, with conclusions given in Sect. 7.

2 Averaging kernel selection

2.1 MOPITT

For the CO AKs, we use measurements from MOPITT on EOS-Terra, which is in a Sun-synchronous polar low-Earth orbit (LEO) with ∼ 10:30 and ∼ 22:30 local time (LT) Equator crossing. The MOPITT instrument uses correlation radiometry (e.g., Tolton and Drummond, 1997; Drummond et al., 2010) to detect atmospheric CO absorption. Here we use multispectral CO retrievals designated as MOPITT V5J data (Deeter et al., 2012, 2013). The averaging kernels and corresponding state data used for the training and test sets are selected from land-only, day-only observations from 25 to 50° N, −125 to −75° E in 2006 (representing all months). To ensure significant measurement information in the retrievals, data are filtered for DFS > 1.0, cloud index $= 2$ (where both MOPITT and MODIS indicate a clear pixel) and the signal-to-noise ratio (SNR) for channel 6D > 10. We also select scenes that were processed with input water vapor profiles (an interferent gas in the CO retrieval) from NOAA's National Centers for Environmental Prediction (NCEP) operational analysis meteorological fields and not the backup climatology that is used when NCEP data are not available. For MOPITT CO we use AKs for parameters in $\log_{10}(q(z))$, where q is species abundance and z is the vertical coordinate.

The results shown here are only for MOPITT observations with surface pressure > 900 hPa. (Lower surface pressures must be treated separately, which we have also tested with this method.) MOPITT retrievals of CO profiles are reported on layers of a vertical pressure grid. For MOPITT data with surface pressure > 900 hPa, the AK, $\mathbf{A}$, is a 10×10 matrix corresponding to 100 hPa layers with lower layer boundaries from the surface to 100 hPa (listed in Table 4). As an indication of the measurement sensitivity in the lowermost troposphere (lowest 3 layers), we compute the "surface DFS" from $\Sigma\, \mathbf{A}_{ii}$ where $i = 1$ to 3. Figure 1 shows how this quantity varies for MOPITT 2006 CONUS observations and Fig. 2 shows the MOPITT 2006 CONUS average AK along with AK rows for the surface and 500 hPa for individual observations. The large AK variability shown in Figs. 1 and 2 demonstrates why a single average for the AK would not represent the range of sensitivity to near-surface CO.

2.2 TES-OMI

TES is a TIR Fourier transform spectrometer (FTS) with $0.1\,\mathrm{cm}^{-1}$ spectral resolution over 650 to $2250\,\mathrm{cm}^{-1}$ for

operational nadir observations (Beer, 2006). OMI is a nadir-viewing imaging spectrometer that measures backscattered solar radiation in the ultraviolet–visible (UV–VIS) wavelength range from 270–500 nm (Levelt et al., 2006). Both TES and OMI are on-board the EOS-Aura platform in a Sun-synchronous LEO with ∼ 13:40 ascending node Equator crossing time. The combined TES/OMI retrieval, described in Fu et al. (2013), uses O_3 absorption around 9.6 µm in the TIR and 270–330 nm in the UV. Although these retrievals are not yet performed operationally, beta-version retrievals from TES and OMI observations taken during August 2006 covering the CONUS area were available for testing this prediction method. We selected land-only, day-only, cloud-free observations from 23 to 55° N, −128 to −68° E. Observations are considered cloud-free if the TES-only retrieval reported an effective cloud optical depth < 0.1. For TES-OMI O_3, we use AKs for parameters in $\ln(q(z))$, where q is species abundance and z is the vertical coordinate.

Although the TES-OMI O_3 profiles and AKs are reported on a 64-level pressure grid from 1000 to 0.1 hPa, we found that using only the first 10 levels (surface to 421.7 hPa) gave the most robust performance with a multiple regression fit (i.e., successful inversions). These lowest levels represent the vertical range in the troposphere with the most variability in retrieval sensitivity and therefore of most interest for this study. For pressure levels from 383 to 10 hPa, we apply the average AK for this August 2006 CONUS data in testing our results. Using only retrievals with surface pressure > 910 hPa, we have 10 × 10 matrices for the TES/OMI AKs corresponding to pressure levels listed in Table 4. The spatial distribution of TES/OMI sensitivity to O_3 in the lowermost troposphere from the surface to 600 hPa, computed with $\Sigma \mathbf{A}_{ii}$ where $i = 1$ to 6, is shown in Fig. 3. Figure 4 shows the TES/OMI CONUS average AK for pressures from the surface to 10 hPa and from surface to 421.7 hPa, which are used for this study. Figure 4 also shows AK rows for the surface and 510.9 hPa level for individual observations to demonstrate the variability in TES-OMI sensitivity over the CONUS scenes.

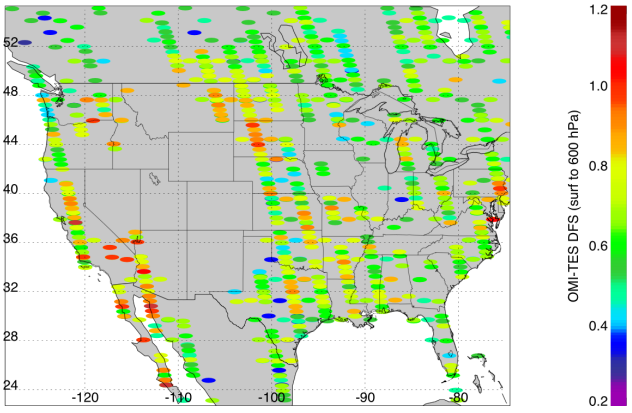

Fig. 3. TES-OMI sensitivity to lower tropospheric O_3, given by the trace of the AK for the lowest 5 layers. Only land scenes with surface pressure > 900 hPa are included; each oval represents a single observation.

3 SVD processing of the AK matrix

The number of vertical levels on which tropospheric composition retrievals are performed varies by instrument and, to a certain extent, is somewhat arbitrary. For convenience the retrieval grid may be chosen to match the vertical grid used by the underlying forward model, as is the case with the TES retrieval. It should certainly be of sufficient vertical resolution (i.e., contain sufficient levels) to represent vertical structure in the background error covariance and retrieved profile. However, the number of retrieval levels is usually many more than the DFS of the retrieval, with highly correlated errors as demonstrated by the broad, overlapping rows of the AK. For this reason, we apply an SVD to the averaging kernels we use in our training set for the multiple regression. This has the following advantages for the AK prediction tool: (1) the complexity of the regression is reduced by considering only the most significant orthogonal features of the vertical structure in the AK, and (2) during the OSSE data assimilation step, the assimilation of the leading components of the SVD of the AK mitigates the effects of vertical correlation in the retrieval error covariance. This allows for sequential assimilation of independent retrieval information, without significant information loss, in addition to significantly reducing the data volume (e.g., Joiner and da Silva, 1998; Rodgers, 2000; Segers et al., 2005; Arellano and Edwards, 2013).

Given an AK matrix **A,** we compute the SVD as

$$\mathbf{A} = \mathbf{U}\,\mathbf{\Lambda}\,\mathbf{V}^T, \tag{4}$$

where the columns of **U** and **V** are the left and right singular vectors (respectively) and the elements of **Λ** (diagonal matrix) are the singular values. For this work, we use the SVDC (SVD in C language) routine from Interactive Data Language (IDL, 2012). For MOPITT CONUS CO AKs, the first 2 singular vectors account for 95 % of the variability on average (with 5 % standard deviation) while the first 3 singular vectors account for 99.995 %. Similarly, the TES-OMI O_3 AKs up to 400 hPa can be reproduced with high accuracy by the first 3 leading singular vectors. (Note that for TES-OMI AKs up to 10 hPa, we would need the first 7 leading singular vectors to reproduce the O_3 AK variability through the stratosphere.)

For each **A**, we retain the first 3 ranked singular vectors for **U** and **V**, along with the rotated AK matrix given by $\mathbf{R} = \mathbf{U}^T\,\mathbf{A}$. Since the SVD results have a potential sign ambiguity (Bro et al., 2007), we also test for negative orientation in each of the 3 singular vectors for **U**, **V** and **R**. For example, $p_i^U = -1$ if the absolute value of the minimum of $\mathbf{U}_{i,k}$ is larger than the maximum value of $\mathbf{U}_{i,k}$, where $i = 1$, 2 or 3

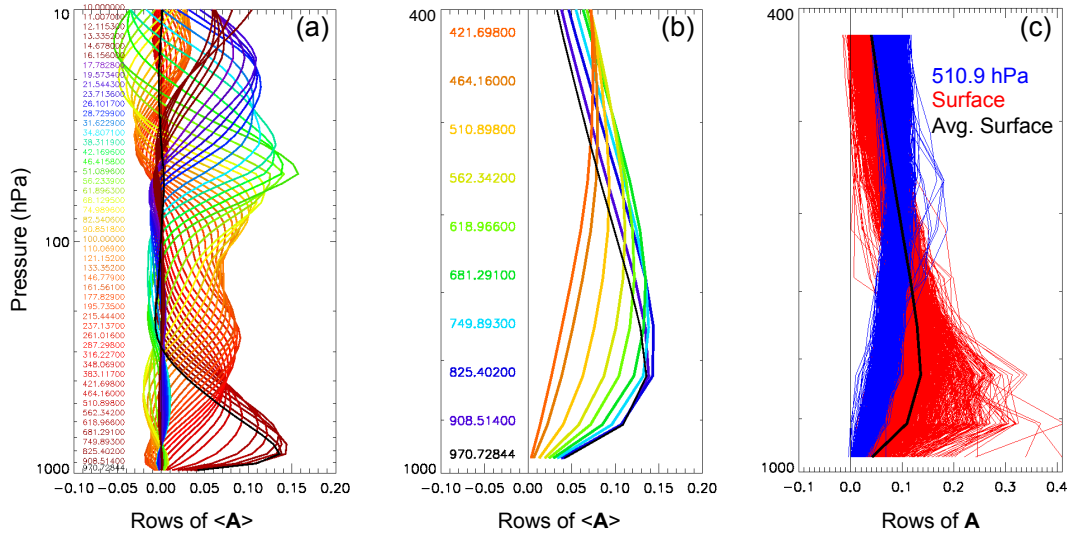

Fig. 4. TES-OMI O_3 AKs for August 2006 CONUS. **(a)** CONUS average AK from surface to 10 hPa, with colors corresponding to pressure levels indicated on the left. **(b)** CONUS average AK from surface to 421 mb. **(c)** Individual AKs for 906 CONUS observations for the surface (red lines) and 510.9 hPa (blue lines) and average surface AK (black line).

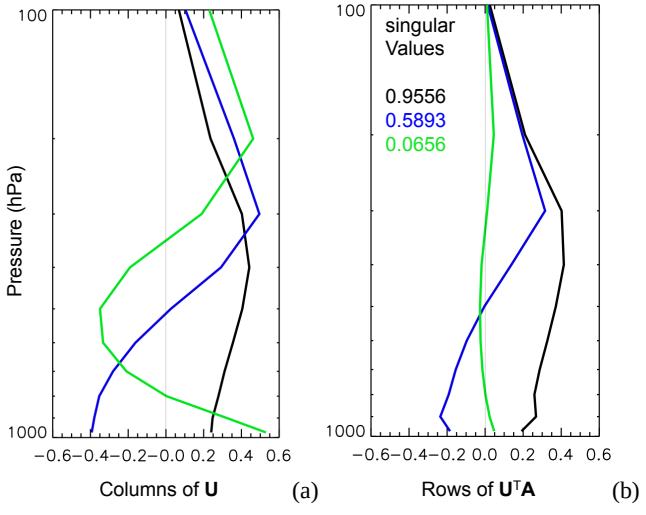

Fig. 5. (a) Left singular vector (**U**) from the SVD of the MOPITT 2006 CONUS average CO AK (first three ranked columns). **(b)** first three rows of the rotated average AK (R) with corresponding singular values.

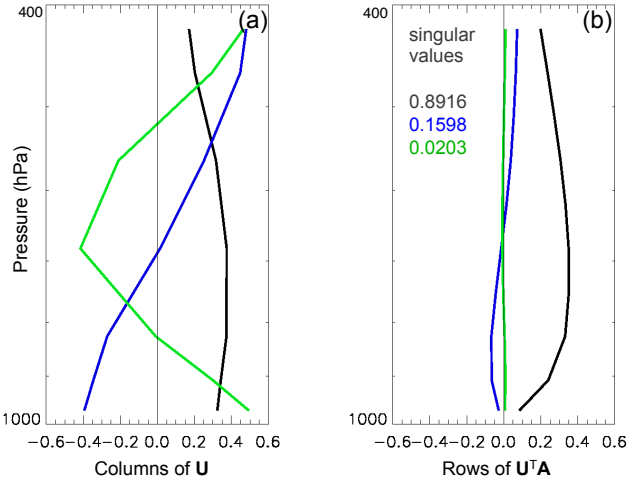

Fig. 6. Same as Fig. 5, but for the SVD of the TES-OMI CONUS average O_3 AK.

and k is the column index; otherwise, $p_i^U = 1$. The sign coefficients, p_i^U, p_i^V, and p_i^R, are stored with the i-th singular vectors for each scene.

The averaging kernel prediction scheme used here uses a regression function. Similar to artificial neural networks terminology, we call the dataset used to infer the coefficients of the regression function the "training set" and the dataset that provides a separate set of predictors and true AKs the "test set". The training and test datasets of MOPITT and TES-OMI AKs are determined by a simple selection of even/odd observation indices, and we have confirmed that no spatial bias is introduced. Corresponding state parameters (described below) for each MOPITT and TES-OMI retrieval are also stored with the training and test sets. As a reference case, we compute the average AK for the region of interest (i.e., CONUS for this study). This provides a comparison for evaluation of the predicted AK variability, described in Sect. 6, as well as a mean subtraction reference for the training set cases. We compute the SVD and sign coefficients for the average AK, and store the differences of the **U**, **V** and **R** singular vectors of each observation of the training set with respect to the average AK singular vectors, thereby restricting our fit algorithm to the vertical structures that are variable

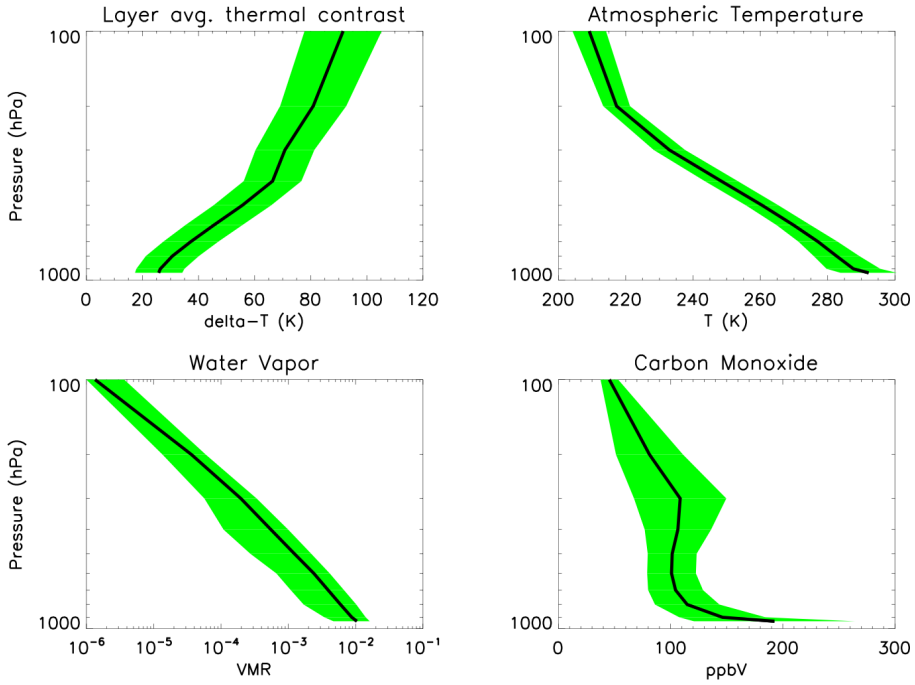

Fig. 7. Pressure-dependent state parameters for MOPITT CONUS 2006 training set. Black lines indicate mean values. Green areas show mean ± standard deviation.

Table 1. Non-pressure-dependent parameters for MOPITT CO AK multiple regression f (2006 CONUS data sample, all seasons, number of scenes in training set = 15 952).

Parameter	Mean	Std. deviation	Min. value	Max. value
θ_sza (deg.)	39.2	13.8	14.5	74.4
SNR (ch. 6D)	88.3	64.7	10.0	767
Emissivity	0.956	0.04	0.78	1.0
Latitude (deg.)	38.1	6.3	25.0	50.0
T_srf (K)	287.6	15.3	217.5	334.6
ΔP_srf (hPa)	0.0	31.4	−72.7	59.4
CO column (10^{18} molecules cm^{-2})	2.21	0.36	0.95	6.91

Table 2. Non-pressure-dependent parameters for TES-OMI O_3 AK multiple regression fit (August 2006 CONUS data, number of scenes in training set = 453).

Parameter	Mean	Std. deviation	Min. value	Max. value
θ_sza (deg.)	32.3	6.4	20.5	48.1
Albedo (OMI ch.2)	0.050	0.025	5.e-5	0.16
Emissivity	0.986	0.012	0.931	1.0
Latitude (deg.)	41.5	8.6	23.1	55.7
T_surface (K)	303.5	9.8	280.0	328.9
ΔP_surface (hPa)	0.0	27.3	−60.8	30.2
Tropopause pressure (hPa)	141.5	45.0	75.0	261.0
Trop. O_3 column (10^{18} molecules cm^{-2})	1.36	0.25	0.79	3.27

from the average AK structure. Figures 5 and 6 show the leading 3 columns of the left singular vector (**U**) and rows of the rotated AK (**R**) along with singular values for the SVDs of the average CONUS AKs for MOPITT and TES-OMI, respectively.

4 The multiple regression AK prediction tool

For the training set of average AK-subtracted, leading 3 singular vectors of **U**, **V**, and **R**, at each pressure in the 10-level grid, we perform a multiple regression (MR) fit with predictors derived from the corresponding state parameters included with the retrievals. Here we use the IDL routine REGRESS (IDL, 2012) to perform the following fit over the training set for each singular vector at each pressure denoted by y_i:

$$y_i = c + a_1 x_{i,1} + a_2 x_{i,2} + \ldots + a_N x_{i,N} \quad (5)$$

with resulting constant c and N coefficients a, for N predictors x from the i-th observation in the training set. Some predictors (x) are pressure-dependent and some are independent of pressure. In selecting predictors, we first considered the more important predictors used in the regression technique for parametrizing MOPITT forward model transmittances (Edwards et al., 1999). Pressure-independent predictors are listed in Table 1 for MOPITT and Table 2 for

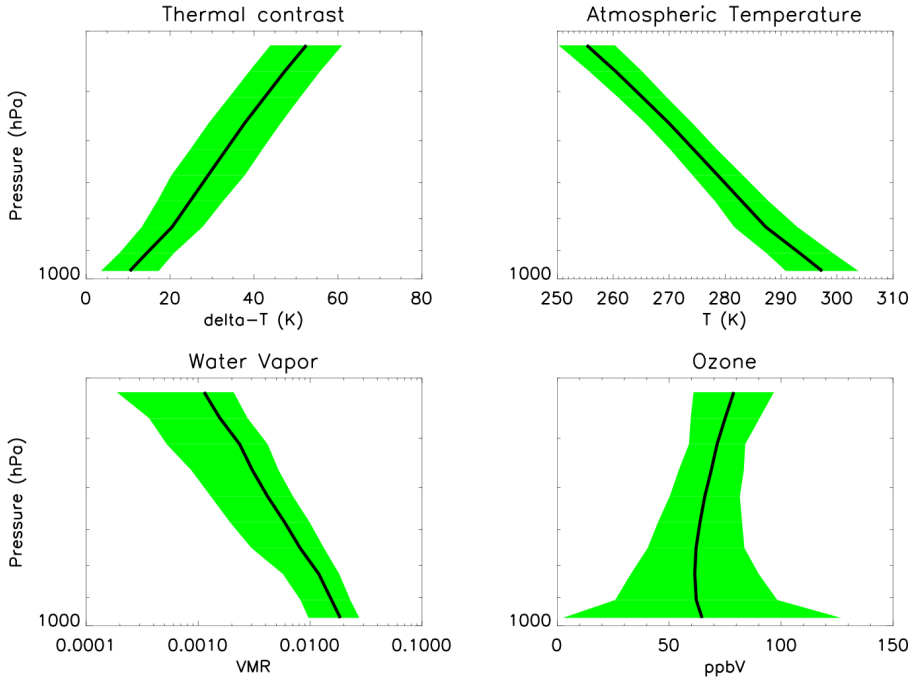

Fig. 8. Same as Fig. 7 but for TES-OMI pressure-dependent state parameters.

TES-OMI retrievals, with mean, standard deviation, minimum and maximum values given to indicate the ranges of values covered by the training datasets. Pressure-dependent predictors, atmospheric temperature ($T(z)$), thermal contrast ($\Delta T(z) = T_{\text{surface}} - T(z)$), water vapor volume mixing ratio (VMR) and retrieval species (CO or O_3) VMR, are plotted in Fig. 7 for MOPITT and Fig. 8 for TES-OMI. Here thermal contrast is defined with layer average temperatures, while temperature profiles correspond to pressure levels. For MOPITT retrievals, we use the SNR for the difference signals in the 2.3 µm NIR channel (ch 6D) as a proxy for albedo. For OSSEs with variable albedo, these could be scaled to match the range shown for SNR (ch 6D). Along with the predictors listed in Tables 1 and 2, we also use MR predictors defined from combined parameters such as ΔT^2, $\cos(\theta_{\text{sza}})/\log_{10}(\text{CO})$ and $\Delta T/\log_{10}(\text{CO})$. All predictors were tested individually and all provide improvements to the fit, but with varying degrees of significance (see below). The resulting coefficients from the training set MR are stored. These are used below in the evaluation of the tool in for the test dataset AKs and corresponding predictors derived from their physical parameters.

4.1 MR predictor significance

The AK, given by Eq. (2), has contributions from instrument sensitivity through the Jacobian (weighting function) matrix $\mathbf{K}$ and measurement error $\mathbf{S}_e$ (Rodgers, 2000). For a constant a priori error covariance or other constraint, $\mathbf{S}_a$, we expect the parameters that affect variations in the AK to fall within two basic categories: weighting functions and SNR. Since we are considering existing instruments, we are not examining a wide range in SNR. Therefore, we expect much of the variation in our regression to be explained by parameters that affect the weighting functions such as T, ΔT, retrieval species abundance (CO or O_3), water vapor, etc. Since MOPITT uses $\boldsymbol{x} = \log_{10}(\text{VMR})$ in the CO retrieval and TES/OMI uses $\boldsymbol{x} = \ln(\text{VMR})$ for O_3, following Eq. (3), both of these produce weighting functions that have a dependence on $q(z)$ (i.e., VMR) with increasing magnitude for increasing VMR:

$$\frac{\partial \boldsymbol{F}}{\partial \log_{10} q(z)} = \left(\log_{10} e\right) q(z) \frac{\partial \boldsymbol{F}}{\partial q(z)}$$

$$\text{and} \quad \frac{\partial \boldsymbol{F}}{\partial \ln q(z)} = q(z) \frac{\partial \boldsymbol{F}}{\partial q(z)}. \tag{6}$$

Since the MR predictors are not always independent of each other, we need a method to assess their contributions to the MR fit. To evaluate whether an individual predictor improves or degrades the overall performance of the fit, we use the error metrics described in Sect. 6, applied to the cases where each predictor is removed, one at a time. For the MOPITT AKs, the most important predictor for accuracy in the lowest levels (highest pressures) is ΔP_srf. However, this is an artifact of how we have defined our vertical grid boundaries and reference to the average CONUS AK. The most significant physical predictors are CO column and T (temperature profile), followed by CO profile, ΔT^2 and SNR (ch 6D). Other predictors such as water vapor VMR and surface emissivity added almost negligible improvements to the fit, which is to be expected in the case of MOPITT since these parameters

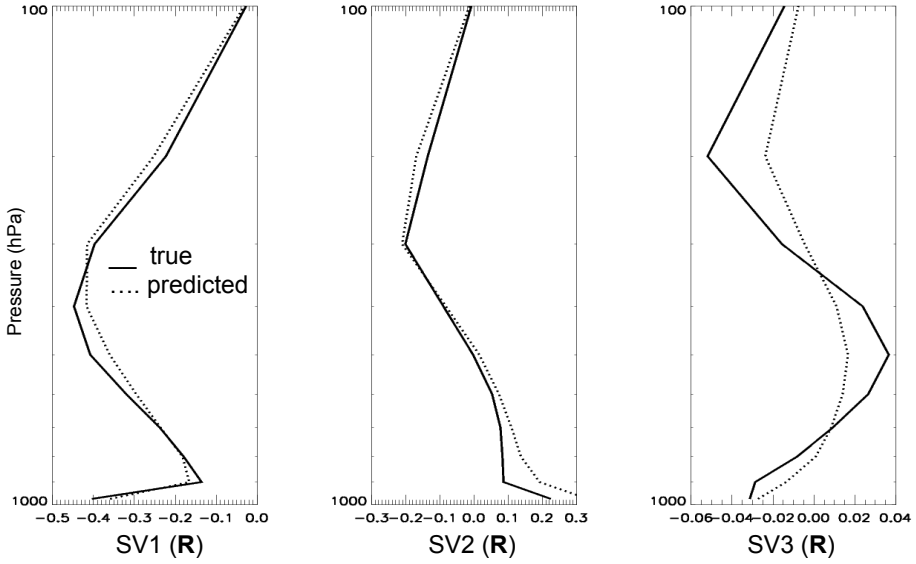

Fig. 9. Example of a test case to evaluate the prediction for singular vectors (SVs) for the rotated AK (R) for a single MOPITT observation. Solid lines indicate the true rows of R from the test case observation; dotted lines indicate the results of the prediction using MR coefficients from the training set and the state parameters from the test case observation as input.

have little impact on the weighting functions or SNR of a gas filter correlation radiometer. This is due to the fact that their radiative effect is uncorrelated with that of CO and, to first order, cancels from the radiance signals used by the retrieval.

For the TES-OMI retrievals, the most important predictors (in order) are O_3 profile, ΔP_srf and T. As for MOPITT, the dependence on ΔP_srf is an artifact of how we specify our grid and reference AK. These are followed by tropospheric O_3 column, surface temperature (T_srf), tropopause pressure and ΔT^2. We found that including water vapor and solar zenith angle (sza) actually degraded the fit in the TES-OMI cases, for reasons we do not fully understand, but possibly because our training set was limited to 453 observations and did not have a sufficient range in these parameters.

Table 3 lists the linear Pearson correlation coefficients for surface DFS (trace of the AK for the 3 lowest layers) with the predictors that are most important to the MR fit. For both MOPITT and TES-OMI, we can conclude that MR dependence on either column amount or VMR is more important than T or ΔT. For MOPITT TIR-only retrievals, surface DFS has significantly more correlation with ΔT^2 than the multispectral cases, but it is still less than the correlation with CO column. Although TIR-only retrievals rely on sufficient thermal contrast for retrieval sensitivity in the lower troposphere (Deeter et al., 2007; Clerbaux et al., 2009), by selecting only retrievals with DFS > 1, we may have limited the range of thermal contrast such that the correlation with CO column (due to the use of log(VMR) parameters) is more dominant.

5 Prediction of averaging kernels for the test dataset

Using the coefficients from the MR and predictors from a test retrieval case, we create $\mathbf{U}_{\mathrm{MR}}$ and reconstruct the predicted left singular vector $\mathbf{U}_{\mathrm{pred}}$ with

$$\mathbf{U}_{\mathrm{pred}} = \mathbf{U}_{\mathrm{MR}} + p^{U}_{\mathrm{avg}}\,\mathbf{U}_{\mathrm{avg}}, \tag{7}$$

where $\mathbf{U}_{\mathrm{avg}}$ is the SVD of the average CONUS AK, with sign p^{U}_{avg} stored with the coefficients. Corresponding operations are performed to obtain $\mathbf{V}_{\mathrm{pred}}$ and $\mathbf{R}_{\mathrm{pred}}$. Since the actual SVD-transformed AKs for each test case observation are also available, a direct comparison of the true and predicted quantities can be made to evaluate the accuracy of the technique. Figure 9 shows an example of the predicted singular vectors for $\mathbf{R}$ compared to the true $\mathbf{R}$ for a single test case observation from MOPITT. Reconstructed singular values are estimated using

$$\Lambda_{ii} = \mathrm{sqrt}\left(\Sigma_k \left[\mathbf{R}_{\mathrm{pred}}(i,k)\right]^2 / \Sigma_k \left[\mathbf{U}_{\mathrm{pred}}(i,k)\right]^2\right), \tag{8}$$

where $i = 1$, 2 or 3 and k is the column index. Using original matrices $\mathbf{R}$ and $\mathbf{U}$, the diagonal values of Λ are reproduced exactly with Eq. (8), while $\mathbf{R}_{\mathrm{pred}}$ and $\mathbf{U}_{\mathrm{pred}}$ produce reasonable approximations to the singular values in order to reconstruct a full 10×10 AK matrix with

$$\mathbf{A}_{\mathrm{pred}} = \mathbf{U}_{\mathrm{pred}}\,\Lambda\,\mathbf{V}^{T}_{\mathrm{pred}}. \tag{9}$$

The MR coefficients are used to calculate $\mathbf{U}_{\mathrm{pred}}$, $\mathbf{V}_{\mathrm{pred}}$ and $\mathbf{R}_{\mathrm{pred}}$ for each set of state parameters corresponding to the AKs in the test data, and Eq. (9) gives a predicted AK that can be compared to the true AK from the test set. Figure 10

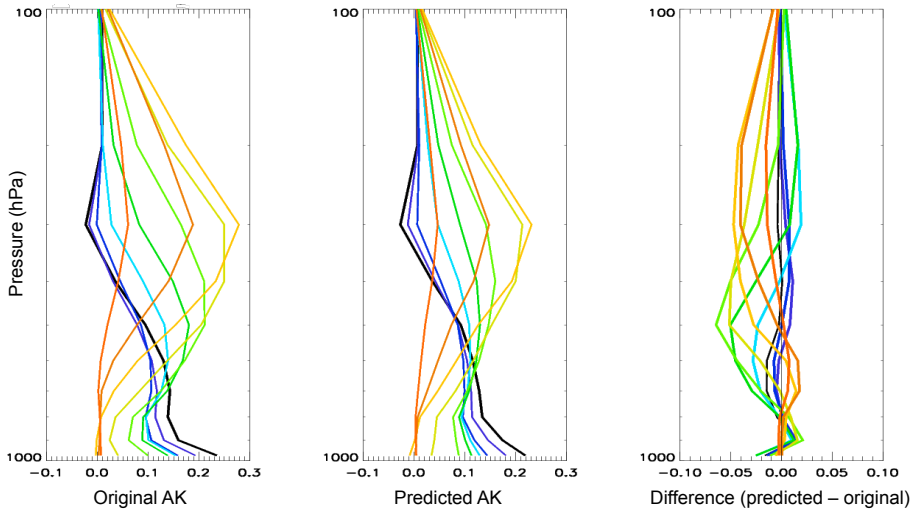

Fig. 10. Example of original MOPITT test case AK and corresponding predicted AK using the results of the MR prediction shown in Fig. 9 to reconstruct the predicted AK. Difference between predicted and original AKs is shown on the right.

shows the predicted AK compared to the true AK for the same MOPITT test case example shown in Fig. 9. Figures 11 and 12 show a test case example for TES-OMI with predicted singular vectors for **R** and reconstructed AK compared to the true values. We compare the average of test case AKs to the average of predicted AKs for MOPITT in Fig. 13 and for TES-OMI in Fig. 14.

6 Evaluation metrics and results

As discussed in Sect. 1, chemical OSSEs to date have usually only considered a very limited number of AK conditions (e.g., two representative average AKs for land and ocean scenes). In order to compare the performance of our individual scene-dependent predicted AKs to a single CONUS average AK, we established a metric for the error in VMR given by the difference between a reference profile that is smoothed by either the predicted AK ($\mathbf{A}_{\text{pred}}$) or CONUS average AK ($\mathbf{A}_{\text{cavg}}$) and the same reference profile smoothed by the true AK ($\mathbf{A}_{\text{true}}$) from each test case. For MOPITT CO, we compute the following for each test case.

$$\boldsymbol{x}_{\text{true}} = \log_{10}\left(\boldsymbol{CO}_{\text{apr}}\right) + \mathbf{A}_{\text{true}}\left[\log_{10}\left(\boldsymbol{CO}_{\text{ref}}\right) - \log_{10}\left(\boldsymbol{CO}_{\text{apr}}\right)\right] \quad (10)$$

$$\boldsymbol{x}_{\text{cavg}} = \log_{10}\left(\boldsymbol{CO}_{\text{apr}}\right) + \mathbf{A}_{\text{cavg}}\left[\log_{10}\left(\boldsymbol{CO}_{\text{ref}}\right) - \log_{10}\left(\boldsymbol{CO}_{\text{apr}}\right)\right] \quad (11)$$

$$\boldsymbol{x}_{\text{pred}} = \log_{10}\left(\boldsymbol{CO}_{\text{apr}}\right) + \mathbf{A}_{\text{pred}}\left[\log_{10}\left(\boldsymbol{CO}_{\text{ref}}\right) - \log_{10}\left(\boldsymbol{CO}_{\text{apr}}\right)\right] \quad (12)$$

$$\Delta\boldsymbol{CO}_{\text{cavg}} = 10^{\wedge}\left(\boldsymbol{x}_{\text{cavg}}\right) - 10^{\wedge}\left(\boldsymbol{x}_{\text{true}}\right) \quad (13)$$

$$\Delta\boldsymbol{CO}_{\text{pred}} = 10^{\wedge}\left(\boldsymbol{x}_{\text{pred}}\right) - 10^{\wedge}\left(\boldsymbol{x}_{\text{true}}\right), \quad (14)$$

where $\boldsymbol{CO}_{\text{apr}}$ is a global average profile and $\boldsymbol{CO}_{\text{ref}}$ is a CONUS average profile, both from the climatology used in MOPITT retrievals (Deeter et al., 2010). For TES-OMI O_3 test cases, we use equations similar to Eqs. (10)–(14), except with ln(O_3 VMR), and with an a priori profile for the Pacific Ocean and a reference profile for CONUS, from the climatology used in the TES-OMI retrievals (Fu et al., 2013), where we have added 50 ppb at the lowest 3 levels to approximate a polluted boundary layer case. Table 4 lists the CO and O_3 a priori and reference profile values.

Histograms of $\Delta\boldsymbol{CO}_{\text{cavg}}$ for each pressure are shown in Fig. 15a. These show that using a CONUS average AK approximation would give small errors in CO for the middle and upper troposphere (pressures below 600 hPa), but would not capture the true sensitivity to CO variability (as compared to the original test case AKs) in the lower troposphere. For the CONUS average AK approximation, only 49 % of the test cases have CO values within 5 ppb of the CO values obtained from using the true AKs in the surface layer. Figure 15b shows histograms of $\Delta\boldsymbol{CO}_{\text{pred}}$ where we see similar performance in the middle and upper troposphere and significant improvements for the CO error in the lower troposphere. For the predicted AKs, the number of cases with CO errors within 5 ppb increases to 82 % in the surface layer.

TES-OMI histograms for ΔO_3 (% errors) are shown in Fig. 16. We use percent error in order to show the performance of the CONUS average and predicted AKs at all pressure levels on the same plot. For the TES-OMI predicted AKs, performance was somewhat worse at pressures below 600 hPa compared to the CONUS average AK. We therefore adopted a hybrid approach of using the predicted AK rows at pressures greater than 600 hPa and the CONUS average AK rows at all lower pressures. Figure 16a shows a broad distribution in O_3 errors for surface to 681 hPa pressure levels when using a CONUS average AK, while in Fig. 16b the error histograms at these same pressure levels have much narrower distributions when using predicted AKs. Figure 17 shows the CONUS average and predicted AK histograms

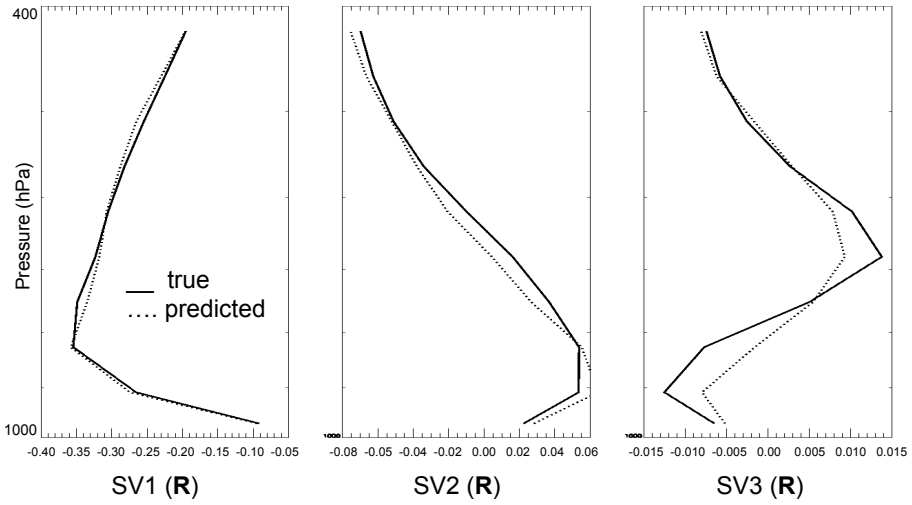

Fig. 11. Same as Fig. 9 but for TES-OMI test case and prediction.

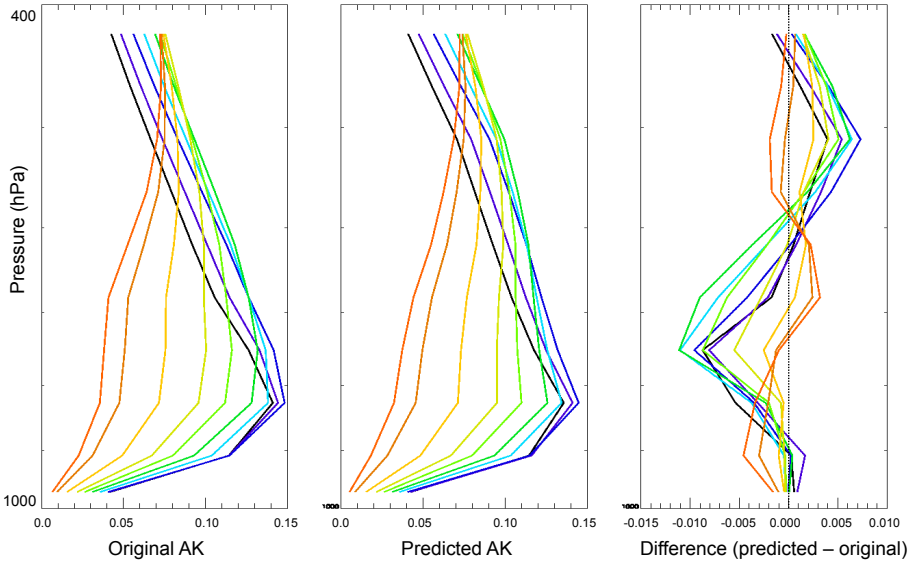

Fig. 12. Same as Fig. 10 but for TES-OMI test case AK and prediction.

computed for O_3 differences in ppb, for surface to 421 hPa pressures.

We note that the shape and mean values in the CO or O_3 error histograms will partially depend on the choice of reference and a priori profiles used for computing this metric. However, here we are testing the relative performance of the predicted AKs compared to the CONUS average AK, which are evaluated using the same a priori and reference profiles. Using this metric, we can test the performance of the predicted AKs when removing predictors from the MR (as discussed in Sect. 4.1) and also show how the predicted AKs improve errors in the lower troposphere over the baseline approximation of using a CONUS average AK in an OSSE (Figs. 15–17).

7 Summary and conclusions

We have demonstrated a method for predicting scene-dependent, cloud-free AKs for tropospheric retrievals of CO and O_3 using coefficients from a multiple regression fit of AK singular vectors and predictors formed from the state parameters of multispectral observations. This tool provides a fast approximation for the instrument simulator component of a chemical OSSE that could be used for determining how much information is added from the observational perspective of GEO compared to existing satellite measurement capability from LEO. We used CONUS observations from existing LEO satellite measurements of CO (from Terra/MOPITT) and O_3 (from Aura/TES and OMI) that have shown increased

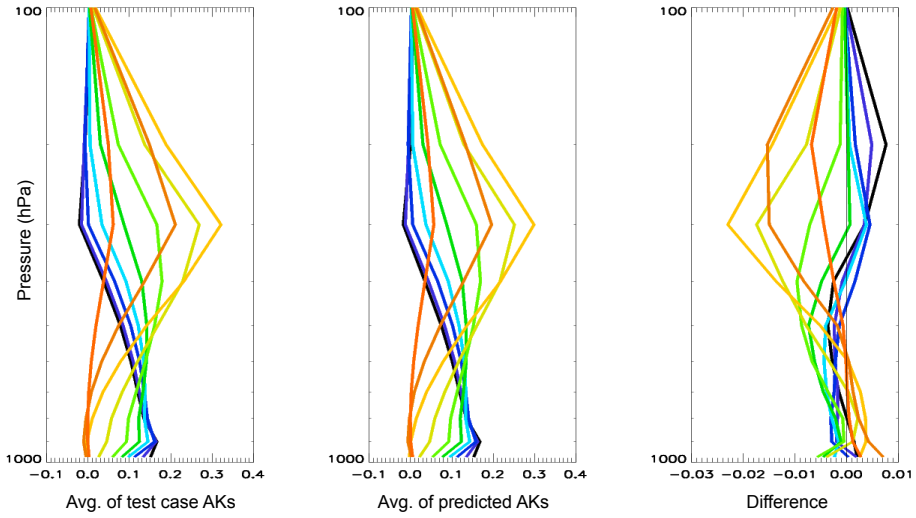

Fig. 13. Comparison of the average CO AK for MOPITT test cases and average of corresponding predicted AKs. Difference between average predicted and average test case AKs is shown on the right.

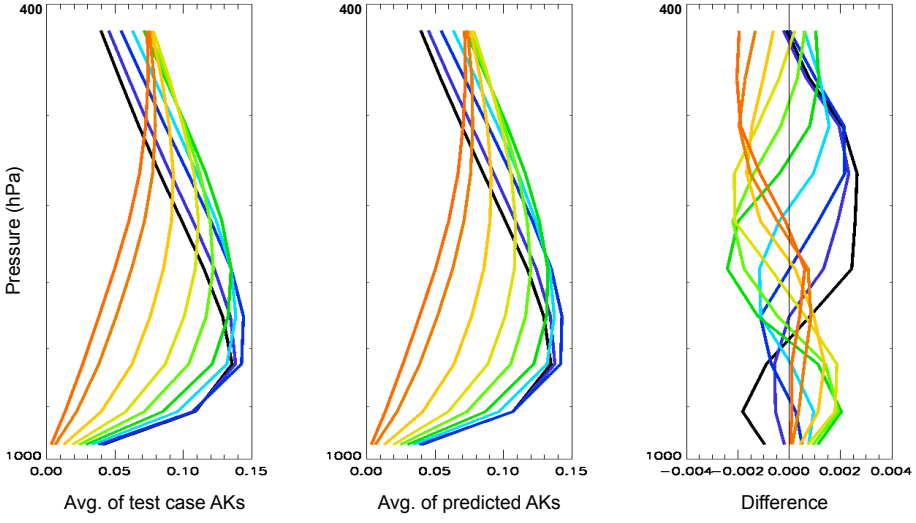

Fig. 14. Same as Fig. 13 but for TES-OMI test cases.

sensitivity to the lower troposphere in some scenes with retrievals that combine multispectral radiances. After applying an SVD to the averaging kernels, we performed a multiple regression fit on the leading three singular vectors of **U**, **V** and rotated AK **R** for our training set of observations. We then used the coefficients of the MR to create predicted AKs using predictors derived from the state parameters of our test observations. By comparing the adjustments to reference CO and O_3 profiles from applying the true, predicted and CONUS average AKs, we evaluated the relative performance of the predicted AK in terms of VMR error. We found that the predictors most important for reproducing the variability in the lowermost troposphere for MOPITT and TES-OMI multispectral AKs were species abundance (column or VMR profiles) followed by temperature and thermal contrast. We have shown that using this AK prediction tool in a chemical OSSE would provide a significant improvement in accuracy compared to an OSSE that uses a single CONUS average AK. For our reference CO and O_3 profiles, the percentage of cases that would have VMR errors less than 5 ppb in the near-surface layer increased from 49 to 82 % for CO and from 65 to 92 % for O_3 from applying the predicted AKs as compared to the CONUS average AK. The next step in this work will be the implementation of the AK prediction tool in the data assimilation environment of chemical OSSEs to evaluate CO and O_3 multispectral retrieval performance for the Decadal Survey GEO-CAPE mission. Subsequent work will explore the extension of the method for the measurement simulation of other GEO-CAPE trace gas and aerosol products.

Table 3. Linear Pearson correlation coefficients for surface DFS (lowest 3 layers) vs. state parameters with highest impact to MR fit. For T_atmos, ΔT^2, and O_3 VMR, the average values for the lowest 3 layers are used.

Parameter	MOPITT surface DFS correlation	TES-OMI surface DFS correlation
ΔP_surface	0.37	0.13
CO total column	0.25	
T_atmos.	−0.22	0.27
ΔT^2	0.03	0.47
Trop. O_3 column		0.42
O_3 VMR		0.76

Table 4. A priori and reference profiles for evaluating CO and O_3 errors in predicted or CONUS average AKs.

MOPITT pressure (hPa)	A priori CO profile (ppb)	Reference CO profile (ppb)	TES-OMI pressure (hPa)	A priori O_3 profile (ppb)	Reference O_3 profile (ppb)
Surface	97.0	131.0	Surface	27.3	98.8
900	90.0	122.0	908.51	32.0	100.0
800	89.0	102.0	825.40	37.6	102.2
700	85.0	95.0	749.89	44.1	55.9
600	82.0	91.0	681.29	51.8	60.1
500	80.0	88.0	618.97	55.3	63.5
400	80.0	86.0	562.34	59.0	67.0
300	78.0	82.0	510.90	61.9	70.2
200	70.0	67.0	464.16	65.1	73.7
100	45.0	42.0	421.70	69.4	78.7

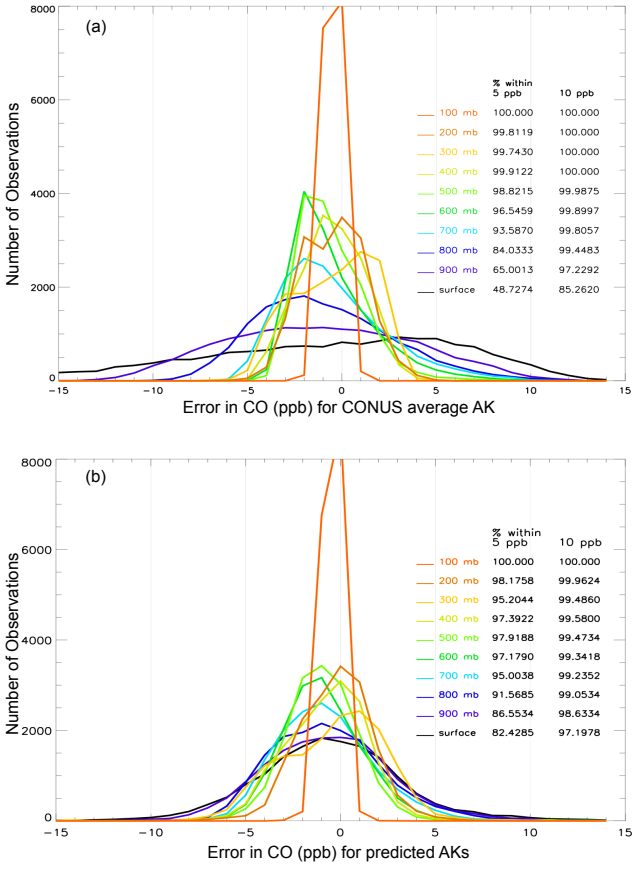

Fig. 15. (a) Performance of CONUS average AK compared to true AKs for MOPITT test cases. **(b)** Performance of predicted AKs compared to true AKs for MOPITT test cases. Histograms of error in CO are plotted for each pressure (indicated by colors on the right). Listed on the far right are the percentages of test cases that fall within 5 and 10 ppb CO error for each pressure. See text for description of error calculation.

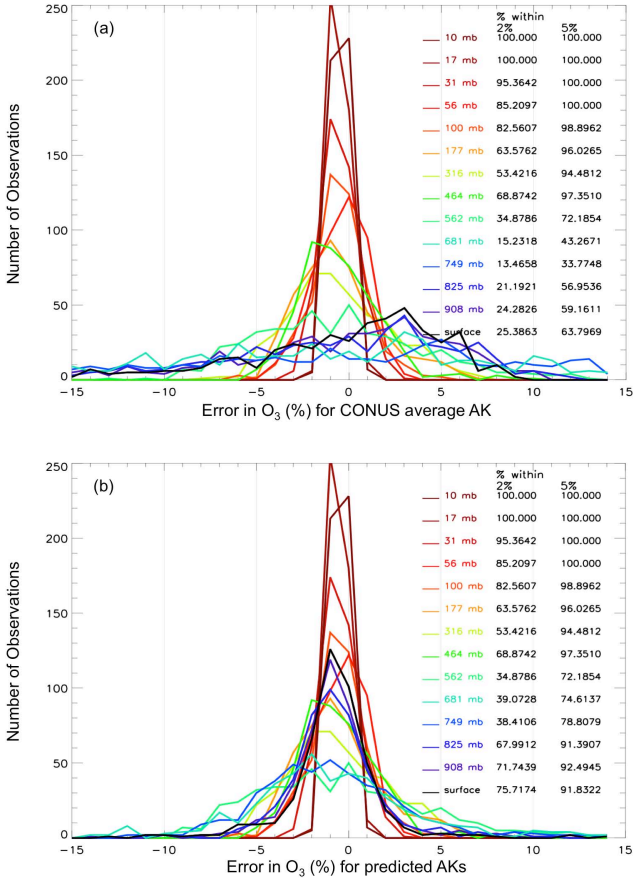

Fig. 16. (a) Performance of CONUS average AK compared to true AKs for TES-OMI test cases. **(b)** Performance of predicted AKs compared to true AKs for TES-OMI test cases. For pressures below 600 hPa, the CONUS average AK is applied. Histograms of error in O_3 are plotted for each pressure (indicated by colors on the right). Listed on the far right are the percentages of test cases that fall within 2 and 5 % O_3 error for each pressure.

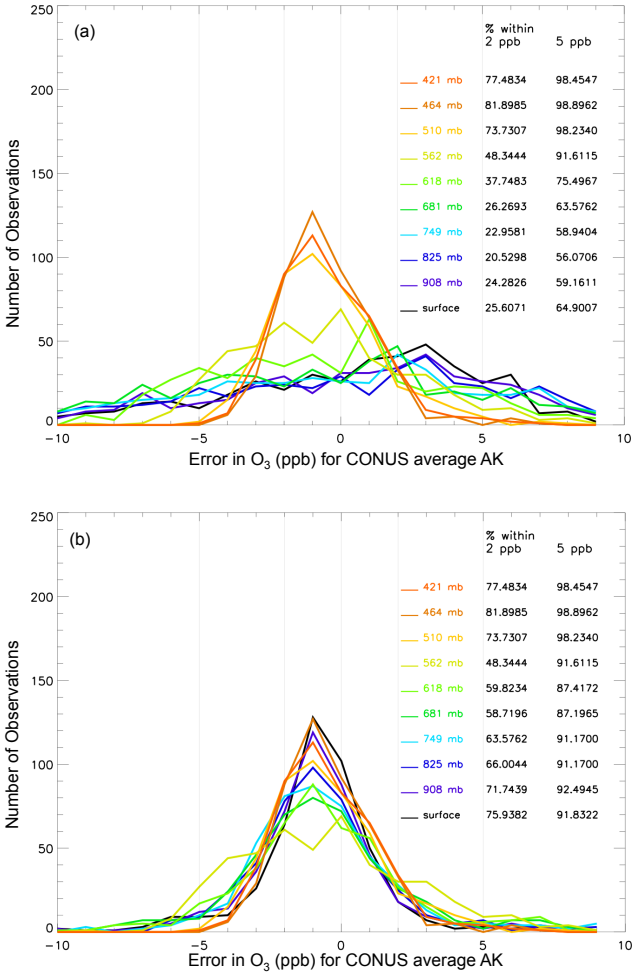

Fig. 17. Same as Fig. 16, but with error expressed in ppb and only showing pressures higher than 400 hPa. **(a)** Performance of CONUS average AK compared to true AKs for TES-OMI test cases. **(b)** Performance of predicted AKs compared to true AKs for TES-OMI test cases. For pressures below 600 hPa, the CONUS average AK is applied. Histograms of O_3 error in ppb are plotted for each pressure (indicated by colors on the right). Listed on the far right are the percentages of test cases that fall within 2 and 5 ppb O_3 error for each pressure.

Acknowledgements. The authors wish to acknowledge support from the National Aeronautics and Space Administration (NASA) Earth Science Division under grants NNX09AH03G, NNX11AG63G and NNX11AI10G. The MOPITT, TES and OMI projects are supported by the National Aeronautics and Space Administration (NASA) Earth Observing System (EOS) Program. The National Center for Atmospheric Research (NCAR) is sponsored by the National Science Foundation.

Edited by: G. Stiller

References

Arellano, A. F. and Edwards, D. P.: Assimilating correlated profile retrievals of chemical constituents in the troposphere, to be submitted to J. Geophys. Res., in preparation, 2013.

Beer, R.: TES on the Aura mission: Scientific objectives, measurements, and analysis overview, IEEE T. Geosci. Remote, 44, 1102–1105, 2006.

Bro, R., Acar, E., and Kolda, T.: Resolving the sign ambiguity in the Singular Value Decomposition, Sandia Report SAND2007-6422, available at: csmr.ca.sandia.gov/~wpk/pubs/bibtgkfiles/SAND2007-6422.pdf (last access: 29 October 2012), 2007.

Claeyman, M., Attié, J.-L., Peuch, V.-H., El Amraoui, L., Lahoz, W. A., Josse, B., Joly, M., Barré, J., Ricaud, P., Massart, S., Piacentini, A., von Clarmann, T., Höpfner, M., Orphal, J., Flaud, J.-M., and Edwards, D. P.: A thermal infrared instrument onboard a geostationary platform for CO and O_3 measurements in the lowermost troposphere: Observing System Simulation Experiments (OSSE), Atmos. Meas. Tech., 4, 1637–1661, doi:10.5194/amt-4-1637-2011, 2011.

Clerbaux, C., Boynard, A., Clarisse, L., George, M., Hadji-Lazaro, J., Herbin, H., Hurtmans, D., Pommier, M., Razavi, A., Turquety, S., Wespes, C., and Coheur, P.-F.: Monitoring of atmospheric composition using the thermal infrared IASI/MetOp sounder, Atmos. Chem. Phys., 9, 6041–6054, doi:10.5194/acp-9-6041-2009, 2009.

Cuesta, J., Eremenko, M., Liu, X., Dufour, G., Cai, Z., Höpfner, M., von Clarmann, T., Sellitto, P., Foret, G., Gaubert, B., Beekmann, M., Orphal, J., Chance, K., Spurr, R., and Flaud, J.-M.: Satellite observation of lowermost tropospheric ozone by multispectral synergism of IASI thermal infrared and GOME-2 ultraviolet measurements, Atmos. Chem. Phys. Discuss., 13, 2955–2995, doi:10.5194/acpd-13-2955-2013, 2013.

Deeter, M. N., Edwards, D. P., Gille, J. C., and Drummond, J. R.: Sensitivity of MOPITT observations to carbon monoxide in the lower troposphere, J. Geophys. Res., 112, 24306, doi:10.1029/2007JD008929, 2007.

Deeter, M. N., Edwards, D. P., Gille, J. C., Emmons, L. K., Francis, G., Ho, S.-P., Mao, D., Masters, D., Worden, H., Drummond, J. R., and Novelli, P.: The MOPITT Version 4 CO Product: Algorithm Enhancements, Validation, and Long-Term Stability, J. Geophys. Res., 115, D07306, doi:10.1029/2009JD013005, 2010.

Deeter, M. N., Worden, H. M., Gille, J. C., Edwards, D. P., Mao, D., and Drummond, J. R.: MOPITT multispectral CO retrievals: Origins and effects of geophysical radiance errors, J. Geophys. Res., 116, D15303, doi:10.1029/2011JD015703, 2011.

Deeter, M. N., Worden, H. M., Edwards, D. P., Gille, J. C., and Andrews, A. E.: Evaluation of MOPITT retrievals of lower-tropospheric carbon monoxide over the United States, J. Geophys. Res., 117, D13306, doi:10.1029/2012JD017553, 2012.

Deeter, M. N., Martínez-Alonso, S., Edwards, D. P., Emmons, L. K., Gille, J. C., Worden, H. M., Pittman, J. V., Daube, B. C., and Wofsy, S. C.: Validation of MOPITT Version 5 thermal-infrared, near-infrared, and multispectral carbon monoxide profile retrievals for 2000–2011, J. Geophys. Res.-Atmos., 118, 1–16, doi:10.1002/jgrd.50272, 2013.

Drummond, J. R., Zou, J., Nichitiu, F., Kar, J., Deschambaut, R., and Hackett, J.: A review of 9-year performance and operation of the MOPITT instrument, J. Adv. Space Res., 45, 760–774, doi:10.1016/j.asr.2009.11.019, 2010.

Edwards, D. P., Halvorson, C. M., and Gille, J. C.: Radiative transfer modeling for the EOS Terra satellite Measurement of Pollution in the Troposphere (MOPITT) instrument, J. Geophys. Res., 104, 16755–16775, 1999.

Edwards, D. P., Arellano Jr., A. F., and Deeter, M. N.: A satellite observation system simulation experiment for carbon monoxide in the lowermost troposphere, J. Geophys. Res., 114, D14304, doi:10.1029/2008JD011375, 2009.

Field, R. D., Risi, C., Schmidt, G. A., Worden, J., Voulgarakis, A., LeGrande, A. N., Sobel, A. H., and Healy, R. J.: A Tropospheric Emission Spectrometer HDO/H_2O retrieval simulator for climate models, Atmos. Chem. Phys., 12, 10485–10504, doi:10.5194/acp-12-10485-2012, 2012.

Fishman, J., Iraci, L. T., Al-Saadi, J., Chance, K., Chavez, F., Chin, M., Coble, P., Davis, C., DiGiacomo, P. M., Edwards, D., Eldering, A., Goes, J., Herman, J., Hu, C., Jacob, D., Jordan, C., Kawa, S. R., Key, R., Liu, X., Lohrenz, S., Mannino, A., Natraj, V., Neil, D., Neu, J., Newchurch, M., Pickering, K., Salisbury, J., Sosik, H., Subramaniam, A., Tzortziou, M., Wang, J., and Wang, M.: The United States' Next Generation of Atmospheric Composition and Coastal Ecosystem Measurements: NASA's Geostationary Coastal and Air Pollution Events (GEO-CAPE) Mission, B. Am. Meteorol. Soc., 93, 1547–1566, doi:10.1175/BAMS-D-11-00201.1, 2012.

Fu, D., Worden, J. R., Liu, X., Kulawik, S. S., Bowman, K. W., and Natraj, V.: Characterization of ozone profiles derived from Aura TES and OMI radiances, Atmos. Chem. Phys., 13, 3445–3462, doi:10.5194/acp-13-3445-2013, 2013.

IDL: Version 8.2 (linux x86_64 m64), (c) 2012, Exelis Visual Information Solutions, Inc., http://www.exelisvis.com/ProductsServices/IDL.aspx (last access: 8 July 2013), 2012.

Joiner, J. and da Silva, A. M.: Efficient methods to assimilate remotely sensed data based on information content, Q. J. Roy. Meteorol. Soc., 124, 1669–1694, 1998.

Landgraf, J. and Hasekamp, O. P.: Retrieval of tropospheric ozone: The synergistic use of thermal infrared emission and ultraviolet reflectivity measurements from space, J. Geophys. Res., 112, D08310, doi:10.1029/2006JD008097, 2007.

Levelt, P. F., Hilsenrath, E., Leppelmeier, G., van den Oord, G. H. J., Bhartia, P. K., Tamminen, J., de Haan, J. F., and Veefkind, J. P.: Scientific objectives of the Ozone Monitoring Instrument, IEEE T. Geosci. Remote, 44, 1199–1208, 2006.

Natraj, V., Liu, X., Kulawik, S., Chance, K., Chatfield, R., Edwards, D. P., Eldering, A., Francis, G., Kurosu, T., Pickering, K., Spurr, R., and Worden, H.: Multispectral sensitivity studies for the retrieval of tropospheric and lowermost tropospheric ozone from simulated clear sky GEO-CAPE measurements, Atmos. Environ., 45, 7151, doi:10.1016/j.atmosenv.2011.09.014, 2011.

Rodgers, C. D.: Inverse Methods for Atmospheric Sounding, Theory and Practice, World Scientific, Singapore, New Jersey, London, Hong Kong, 2000.

Segers, A. J., Eskes, H. J., Van der A, R. J., Van Oss, R. F., and Van Velthoven, P. F. J.: Assimilation of GOME ozone profiles and a global chemical transport model using a Kalman filter with anisotropic covariance, Q. J. Roy. Meteorol. Soc., 131, 477–502, 2005.

Sellitto, P., Dufour, G., Eremenko, M., Cuesta, J., Peuch, V.-H., Eldering, A., Edwards, D. P., and Flaud, J.-M.: The effect of using limited scene-dependent averaging kernels approximations for the implementation of fast Observing System Simulation Experiments targeted on lower tropospheric ozone, Atmos. Meas. Tech. Discuss., 6, 2413–2448, doi:10.5194/amtd-6-2413-2013, 2013.

Tolton, B. T. and Drummond, J. R.: Characterization of the length-modulated radiometer, Appl. Optics, 36, 5409–5419, 1997.

Worden, J., Liu, X., Bowman, K., Chance, K., Beer, R., Eldering, A., Gunson, M., and Worden, H.: Improved Tropospheric Ozone Profile Retrievals Using OMI and TES Radiances, Geophys. Res. Lett., 34, L01809, doi:10.1029/2006GL027806, 2007.

Worden, H. M., Deeter, M. N., Edwards, D. P., Gille, J. C., Drummond, J. R., and Nédélec, P. P.: Observations of near-surface carbon monoxide from space using MOPITT multispectral retrievals, J. Geophys. Res., 115, D18314, doi:10.1029/2010JD014242, 2010.

Zoogman, P., Jacob, D. J., Chance, K., Zhang, L., Le Sager, P., Fiore, A. M., Eldering, A., Liu, X., Natraj, V., and Kulawik, S. S.: Ozone Air Quality Measurement Requirements for a Geostationary Satellite Mission, Atmos. Environ., 45, 7143–7150, doi:10.1016/j.atmosenv.2011.05.058, 2011.